

JefiPIC: A 3-D Full Electromagnetic Particle-in-Cell Simulator Based on Jefimenko's Equations on GPU

Jian-Nan Chen^{1,2}, Jun-Jie Zhang^{1,2,*}, Xue-Ming Li³, Hai-Liang Qiao^{1,2}, and Yong-Tao Zhao⁴

¹ Northwest Institute of Nuclear Technology, Xi'an, 710024, China.

² State Key Laboratory of Intense Pulsed Radiation Simulation and Effect, 710024, China.

³ Institute of Applied Physics and Computational Mathematics, Beijing, 100094, China.

⁴ MOE Key Laboratory for Nonequilibrium Synthesis and Modulation of Condensed Matter, School of Science, Xi'an Jiaotong University, Xi'an, 710049, China.

Abstract. This paper presents a novel 3-D full electromagnetic particle-in-cell (PIC) code called JefiPIC, which uses Jefimenko's equations as the electromagnetic (EM) field solver through a full-space integration method. Leveraging the power of state-of-the-art graphic processing units (GPUs), we have made the challenging integral task of PIC simulations achievable. Our proposed code offers several advantages by utilizing the integral method. Firstly, it offers a natural solution for modeling non-neutral plasmas without the need for pre-processing such as solving Poisson's equation. Secondly, it eliminates the requirement for designing elaborate boundary layers to absorb fields and particles. Thirdly, it maintains the stability of the plasma simulation regardless of the time step chosen. Lastly, it does not require strict charge-conservation particle-to-grid apportionment techniques or electric field divergence amendment algorithms, which are commonly used in finite-difference time-domain (FDTD)-based PIC simulations. To validate the accuracy and advantages of our code, we compared the evolutions of particles and fields in different plasma systems simulated by three other codes. Our results demonstrate that the combination of Jefimenko's equations and the PIC method can produce accurate particle distributions and EM fields in open-boundary plasma systems. Additionally, our code is able to accomplish these computations within an acceptable execution time. This study highlights the effectiveness and efficiency of JefiPIC, showing its potential for advancing plasma simulations.

Key words: particle-in-cell, Jefimenko's equation, plasma simulation, integral method, GPU.

Our code is published at:

1. <https://github.com/Juenjie/JefiPIC>
2. <https://codeocean.com/capsule/5129018/tree>

*Corresponding author. Email addresses: zjacob@mail.ustc.edu.cn (J. Zhang)

1 Introduction

1.1 Background

The particle-in-cell (PIC) method is a commonly used tool in plasma physics. It utilizes macro-particles to describe charged particles in similar phase space states and model the evolution of the particle distribution and electromagnetic field. This method was initially proposed by Dawson in the 1960s [1] to study the Langmuir wave in 1-D electrostatic plasma. Later, Langdon and Birdsall improved the PIC model by incorporating finite-size particles [2] or particle clouds [3], which solved the issue of Coulomb collision between particles. Marder [4] and Villasenor [5] addressed the electric field divergence error in the current-driven method. In the last decade, the teams from P. Gibbon and A.J. Christlieb have separately established the integral-method based PIC through solving the vector and scalar potential functions, which can be employed in electrostatic, magneto-static, and electromagnetic problems and has expanded the study in grid-free plasma simulation [6]-[10]. Currently, PIC is used across various fields, including simulating controlled/laser thermonuclear fusion [11], [12], studying nuclear explosions [13]- [15] and space physics effects [16], and designing vacuum electronic devices [17]- [19].

The PIC method offers an intuitive representation of charged particles, making it easier for researchers to analyze simulated phenomena and data. As a result, numerous commercial software and open-source PIC codes have emerged for decades, including but not limited to Smilei [20], PIConGPU [22], WarpX [21], UNIPIC [23], and EPOCH [12], [24].

The PIC model comprises two primary components. The first part involves updating the dynamics of EM fields according to Maxwell's equations,

$$\varepsilon \frac{\partial \mathbf{E}}{\partial t} = \nabla \times \frac{\mathbf{B}}{\mu} - \mathbf{J}, \quad (1.1)$$

$$\frac{\partial \mathbf{B}}{\partial t} = -\nabla \times \frac{\mathbf{E}}{\mu'}, \quad (1.2)$$

$$\nabla \cdot \mathbf{E} = \frac{\rho}{\varepsilon}, \quad (1.3)$$

$$\nabla \cdot \mathbf{B} = 0, \quad (1.4)$$

where \mathbf{E} and \mathbf{B} represent electric and magnetic fields, ε and μ denote the permittivity and permeability of the medium, ρ and \mathbf{J} are the electric charge density and electric current density.

The second part involves updating the positions and velocities of macro-particles using the Newton-Lorentz force equations of motion,

$$\frac{d}{dt}(\gamma m \mathbf{v}) = q(\mathbf{E} + \mathbf{v} \times \mathbf{B}), \quad (1.5)$$

$$\frac{d}{dt} \mathbf{r} = \mathbf{v}, \quad (1.6)$$

where γ , m , q , \mathbf{r} , and \mathbf{v} represent the relativistic factor, particle's mass, charge, displacement, and velocity, respectively.

After ensuring current continuity,

$$\frac{\partial \rho}{\partial t} + \nabla \cdot \mathbf{J} = 0, \quad (1.7)$$

the electric field divergence Eq. (1.3) is implicitly obtained solely through the first two curl Eqs. (1.1) and (1.2), while Eq. (1.4) holds at all time.

1.2 Motivation

The finite-difference time-domain (FDTD) method [25] is well-suited for computing curl Eqs. (1.1) and (1.2) due to its simplicity and data sparsity. This makes it more advantageous than other methods, such as the finite element method (FEM) [26], [27] that necessitates the design of complex basis functions. Thus, the FDTD method has been employed as the EM solver for several decades. In the FDTD-based PIC framework, it is crucial that the finite-difference implementation of the current continuity Eq. (1.7) should be consistent with that of the electric field \mathbf{E} and magnetic field \mathbf{B} [5]. Furthermore, this current-driven method computes the electrostatic fields indirectly by Eq. (1.7), rather than directly through the diverge Eq. (1.3) [28]. To ensure its accuracy, the current interpolation algorithm is meticulously designed to uphold the charge-conservation law [29]- [32].

In this paper, we present JefiPIC, an alternative PIC method that utilizes Jefimenko's equations [33], [34], the general solution to Maxwell's equations, to compute EM fields in plasma simulations by the integral form. Jefimenko's equations are computationally time-consuming, particularly when used in conjunction with the numerous particles updating in PIC methods. To enhance the performance of this integral simulations, we employ the GPU-based package JefiGPU [35], which directly calculate Jefimenko's equation on the GPU with a high-dimensional integration package ZMCintegral [36]. This approach allows us to efficiently evolve plasma systems within an acceptable execution time. Furthermore, we perform particle motion equations on GPU, making JefiPIC a fully GPU-based plasma simulator. All variables are consistently defined in GPU memory, ensuring swift execution of the simulations. Providing the initial conditions of charged particles (neutral or not) and the background EM fields, our code is supposed to automatically compute the particles' space-time distribution as well as the evolution of EM fields.

Compared to the traditional FDTD-based PIC simulation, our proposed JefiPIC has the following advantages:

a) The numerical stability of the integral eliminates the need for the CFL stability condition [37], a criterion in explicit finite difference methods, to prevent numerical divergence. This provides more flexibility and robustness in selecting the computational time step.

b) Our method does not require the use of complex boundary layers to cut off the propagation of EM fields [38], [39]. Besides, simply 'killing' particle in the boundary layers will not result in unintended charge deposition or errors in the electrostatic components

[40], [41]. Thus, our method is well-suited for describing plasma systems with open boundaries.

c) Our method can handle non-neutral plasma without the need for additional pre-treatments, such as solving the Poisson equation [5], even for those new to the field, making it easier to treat the initial conditions.

d) In JefiPIC, EM fields are precisely calculated by the utilization of both charge and current densities, which strictly adheres to the charge conservation law at every time step. Thus, instead of using strict charge conservation algorithms [30] or implementing electric field divergence amendments [4], [28], the simple linear interpolation method can be employed.

Apart from the above merits, our approach inevitably encounters some drawbacks in its current version. For example, the large computational cost, and inconvenience in dealing with the EM boundaries with matters, etc. We will study these issues to make our code more practical in the future.

The paper is structured as follows. Section 2 outlines the detailed design process of JefiPIC, including the Jefimenko's equations, particle motion, the interpolation method for particles and fields, and the implementation of JefiPIC on GPU. In Section 3, we compare the results obtained from JefiPIC, UNIPIC, EPOCH, and RBG-Maxwell [42], [45] through examining the evolutions of three different plasma systems. We further analyze the advantages of JefiPIC compared to other available codes. Finally, in Section 4, we present our conclusions and discuss future research directions.

2 Algorithm and Implementation

As a PIC method, JefiPIC has a similar architecture to the traditional EM PIC, shown in Figure 1. The method involves four processes: 1) computing EM fields on each grid, 2) solving the field interpolation to calculate the forces on the particles, 3) solving the particle interpolation to allocate the charges on the grids, and 4) updating the particle motion. In this section, we will introduce the details of JefiPIC in the sequence of Jefimenko's equations, particle motion, field and particle interpolation and the implementation on GPU.

2.1 Jefimenko's equations

In JefiPIC, the aim is to compute the EM fields over the entire computational region by the Jefimenko's equations with sources \mathbf{J} and ρ ,

$$\mathbf{E}(\mathbf{r}, t) = \frac{1}{4\pi\epsilon_0} \int \left[\frac{\mathbf{r} - \mathbf{r}'}{|\mathbf{r} - \mathbf{r}'|^3} \rho(\mathbf{r}', t_r) + \frac{\mathbf{r} - \mathbf{r}'}{|\mathbf{r} - \mathbf{r}'|^2} \frac{1}{c} \frac{\partial \rho(\mathbf{r}', t_r)}{\partial t} - \frac{\mathbf{r} - \mathbf{r}'}{|\mathbf{r} - \mathbf{r}'|} \frac{1}{c^2} \frac{\partial \mathbf{J}(\mathbf{r}', t_r)}{\partial t} \right] d^3 \mathbf{r}', \quad (2.1)$$

$$\mathbf{B}(\mathbf{r}, t) = -\frac{\mu_0}{4\pi} \int \left[\frac{\mathbf{r} - \mathbf{r}'}{|\mathbf{r} - \mathbf{r}'|^3} \times \mathbf{J}(\mathbf{r}', t_r) + \frac{\mathbf{r} - \mathbf{r}'}{|\mathbf{r} - \mathbf{r}'|^2} \times \frac{1}{c} \frac{\partial \mathbf{J}(\mathbf{r}', t_r)}{\partial t} \right] d^3 \mathbf{r}', \quad (2.2)$$

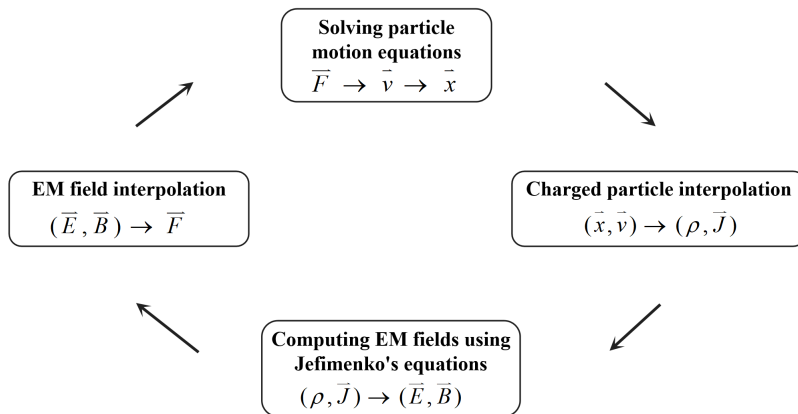


Figure 1: Process diagram for JefiPIC simulation. The overall computational architecture is similar to traditional PIC methods, except for the use of a different EM field solver and the negligible consideration of EM field and particle boundary issues.

$$t_r = t - |\mathbf{r} - \mathbf{r}'|/c, \quad (2.3)$$

where (\mathbf{r}, t) represents the space-time point in the computational region, while $\mathbf{r} = (x, y, z)$ and $\mathbf{r}' = (x', y', z')$ separately refer to the displacements of the EM fields and sources. For numerical computation, we divide the computational region into the same structured cuboid grids. All the EM quantities \mathbf{J} , ρ , \mathbf{E} and \mathbf{B} are defined at the center of the grids. To perform integrations numerically, Eqs. (2.1) to (2.3) are discretized as,

$$\begin{aligned} \mathbf{E}(\mathbf{r}_{I,J,K}, t^n) = & \frac{dx' dy' dz'}{4\pi\epsilon_0} \sum_{i,j,k} \left[\frac{\mathbf{r}_{I,J,K} - \mathbf{r}'_{i,j,k}}{|\mathbf{r}_{I,J,K} - \mathbf{r}'_{i,j,k}|^3} \rho(\mathbf{r}'_{i,j,k}, t_r) \right. \\ & + \frac{\mathbf{r}_{I,J,K} - \mathbf{r}'_{i,j,k}}{|\mathbf{r}_{I,J,K} - \mathbf{r}'_{i,j,k}|^2} \frac{1}{c} \frac{\rho(\mathbf{r}'_{i,j,k}, t_r) - \rho(\mathbf{r}'_{i,j,k}, t_r - dt)}{dt} \\ & \left. - \frac{1}{|\mathbf{r}_{I,J,K} - \mathbf{r}'_{i,j,k}|} \frac{1}{c^2} \frac{\mathbf{J}(\mathbf{r}'_{i,j,k}, t_r) - \mathbf{J}(\mathbf{r}'_{i,j,k}, t_r - dt)}{dt} \right], \end{aligned} \quad (2.4)$$

$$\begin{aligned} \mathbf{B}(\mathbf{r}_{I,J,K}, t^n) = & -\mu_0 \frac{dx' dy' dz'}{4\pi} \sum_{i,j,k} \left[\frac{\mathbf{r}_{I,J,K} - \mathbf{r}'_{i,j,k}}{|\mathbf{r}_{I,J,K} - \mathbf{r}'_{i,j,k}|^3} \times \mathbf{J}(\mathbf{r}'_{i,j,k}, t_r) \right. \\ & \left. + \frac{\mathbf{r}_{I,J,K} - \mathbf{r}'_{i,j,k}}{|\mathbf{r}_{I,J,K} - \mathbf{r}'_{i,j,k}|^2} \times \frac{1}{c} \frac{\mathbf{J}(\mathbf{r}'_{i,j,k}, t_r) - \mathbf{J}(\mathbf{r}'_{i,j,k}, t_r - dt)}{dt} \right], \end{aligned} \quad (2.5)$$

$$t_r = t^n - |\mathbf{r}_{I,J,K} - \mathbf{r}'_{i,j,k}|/c, \quad (2.6)$$

where the subscripts I, J , and K in capital letter of displacement denote the grid index of the unknown EM fields, while the subscripts i, j , and k in lowercase letter of displacement denote the grid index of the source. The superscript n of time refers to the n -th time step, and dx' , dy' , and dz' represent the size of a grid.

2.2 Particle motion

The Newton–Lorentz force Eqs. (1.5) to (1.6) are discretized by the central leap-frog difference method as,

$$\frac{\gamma m(\mathbf{v}^{n+1/2} - \mathbf{v}^{n-1/2})}{dt} = q \left(\mathbf{E}^n + \frac{\mathbf{v}^{n+1/2} + \mathbf{v}^{n-1/2}}{2} \times \mathbf{B}^n \right), \quad (2.7)$$

$$\frac{\mathbf{r}^{n+1} - \mathbf{r}^n}{dt} = \mathbf{v}^{n+1/2}, \quad (2.8)$$

This advancement of velocity involves an implicit equation. To figure out this issue, the Boris particle pusher is employed to separate Eq. (15) into three steps as,

$$\mathbf{v}^- = \mathbf{v}^{n-1/2} + \frac{q\mathbf{E}^n dt}{m} \frac{dt}{2}, \quad (2.9)$$

$$\frac{(\mathbf{v}^+ + \mathbf{v}^-)}{dt} = \frac{q}{2\gamma m} (\mathbf{v}^+ + \mathbf{v}^-) \times \mathbf{B}^n, \quad (2.10)$$

$$\mathbf{v}^{n+1/2} = \mathbf{v}^+ + \frac{q\mathbf{E}^n dt}{m} \frac{dt}{2}, \quad (2.11)$$

where \mathbf{v}^- and \mathbf{v}^+ denote the temporary variables to update the velocity.

2.3 Charge, current and field interpolation method

Based on the discretization of Jefimenko’s equations, the EM fields, current and charge densities all need to be allocated at the center of the grids, which is different from that in the FDTD-based method. The traditional PIC methods usually adopt two kinds of interpolation methods. One approach is the charge-conservation method [46], which generate high-frequency numerical noises in the solenoidal part of current density [4], [28], [47]. The other method is the sample linear interpolation method, which generates less noise [4], but violates the charge conservation law, leading to inaccuracies in electric field. To compensate for this loss in accuracy, electric field correction algorithms must be implemented.

Because the integral-based PIC method calculates the fields directly from the provided current and charge density, JefiPIC avoids the issue of charge conservation. As a result, we can use the first-order linear interpolation method for charge and field allocation in JefiPIC, combining the advantages of both acceptable numerical noise and computational time.

We firstly exhibit how particle interpolation works. In a 3-D model, linear interpolation is achieved through volume-weighted interpolation. For simplicity, we use a 2-D model with the area-weighted interpolation method, as shown in Figure 2. Assuming that there is one particle in the computational region, labeled as a ‘star’. The particle’s charge is distributed to the nearest four center nodes indicated by the circles with indices (i, j) , $(i+1, j)$, $(i, j+1)$ and $(i+1, j+1)$. The area-weighted interpolation method specifies that the allocated charge on each node is proportional to the weight, which is the ratio of the area of its opposite rectangle to that of a single grid. Accordingly, the weight can be

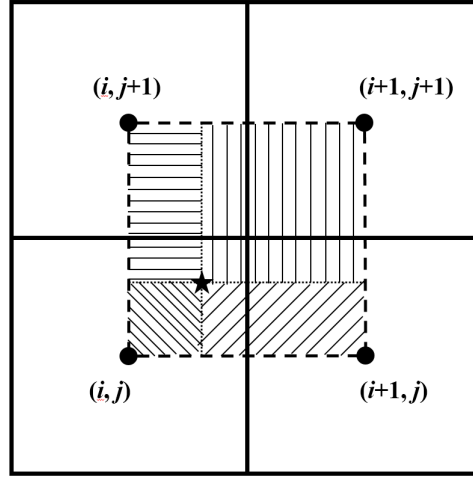


Figure 2: Area-weighted interpolation. The particle is indicated by a 'star' and its charge is interpolated to the four neighboring grids according to the ratio of the corresponding shaded area to a single grid area.

computed by the corresponding volume in 3-D models. The zero-, first- and second-order spline interpolations are as follows,

$$S^{(0)}(x) = 1 \quad \text{for } 0 \leq |x| \leq \Delta \quad (2.12)$$

$$S^{(1)}(x) = \frac{\Delta - x}{\Delta} \quad \text{for } 0 \leq |x| \leq \Delta \quad (2.13)$$

$$S^{(2)}(x) = \begin{cases} \frac{1}{\Delta^2} (-x^2 + \frac{3}{4}\Delta^2) & \text{for } 0 \leq |x| \leq \Delta \\ \frac{1}{8\Delta^2} (2x - 3\Delta)^2 & \text{for } \frac{1}{2}\Delta \leq |x| \leq \frac{3}{2}\Delta \end{cases} \quad (2.14)$$

Since all the physical variables are defined at the center nodes of the grids, we firstly need to find the indices of the grids which the particles belong to,

$$i = \left[\frac{x - 0.5 \cdot dx'}{dx'} \right], j = \left[\frac{y - 0.5 \cdot dy'}{dy'} \right], k = \left[\frac{z - 0.5 \cdot dz'}{dz'} \right], \quad (2.15)$$

where the square bracket means rounding down operation, and x , y , and z are the displacements in the three axes. Following the volume-weighted interpolation method, a particle located at one grid (i, j, k) should interpolate its charge to the adjacent grid nodes as,

$$Q_{i,j,k} = (1 - \alpha)(1 - \beta)(1 - \chi)q,$$

$$Q_{i+1,j,k} = \alpha(1 - \beta)(1 - \chi)q,$$

$$Q_{i,j+1,k} = (1 - \alpha)\beta(1 - \chi)q,$$

$$\begin{aligned}
Q_{i,j,k+1} &= (1-\alpha)(1-\beta)\chi q, \\
Q_{i+1,j+1,k} &= \alpha\beta(1-\chi)q, \\
Q_{i+1,j,k+1} &= \alpha(1-\beta)\chi q, \\
Q_{i,j+1,k+1} &= (1-\alpha)\beta\chi q, \\
Q_{i+1,j+1,k+1} &= \alpha\beta\chi q,
\end{aligned} \tag{2.16}$$

where

$$\alpha = \frac{x - (i+0.5) \cdot dx'}{dx'}, \beta = \frac{y - (j+0.5) \cdot dy'}{dy'}, \chi = \frac{z - (k+0.5) \cdot dz'}{dz'}, \tag{2.17}$$

and q is the charge of the moving particle. We can acquire the charge and current density at node (i,j,k) by,

$$\rho_{i,j,k} = \frac{Q_{i,j,k}}{dx' \cdot dy' \cdot dz'} \tag{2.18}$$

$$(J_{i,j,k,x}, J_{i,j,k,y}, J_{i,j,k,z}) = \rho_{i,j,k} \cdot (v_x, v_y, v_z), \tag{2.19}$$

where v_x , v_y and v_z are the velocities of the particle. The charge and current densities at the corresponding nodes can be obtained according to Eqs. (2.16) to (2.19).

When a particle is located closer to a computational region boundary than half a grid length, it is important to note that the adjacent nodes cannot constitute a full grid. To address this issue, we utilize virtual grids (red grids) to surround the computational region (black grids), as illustrated in Figure 3. We can then implement the same charge interpolation process as displayed in Figure 2, while excluding the computation of charge and current densities on the virtual nodes.

In this part, we will show the field interpolation. Once the EM fields are established on all observation grids, it is required to compute the forces on the particles using the field interpolation method. The field interpolation process works in reverse to that of the charge interpolation method, whereby the weighted EM fields from the adjacent eight grids are summed to calculate the fields acting on a certain particle. The weight of electric field from one grid on the particle is equal to the weight of the particles' charge allocated to that corresponding grid. Thus, the electric field on a particle located in grid (i,j,k) can be evaluated as,

$$\begin{aligned}
\mathbf{E}_{i,j,k}^q &= (1-\alpha)(1-\beta)(1-\chi)\mathbf{E}_{i,j,k} + \alpha(1-\beta)(1-\chi)\mathbf{E}_{i+1,j,k} \\
&+ (1-\alpha)\beta(1-\chi)\mathbf{E}_{i,j+1,k} + (1-\alpha)(1-\beta)\chi\mathbf{E}_{i,j,k+1} \\
&+ \alpha\beta(1-\chi)\mathbf{E}_{i+1,j+1,k} + \alpha(1-\beta)\chi\mathbf{E}_{i+1,j,k+1} \\
&+ (1-\alpha)\beta\chi\mathbf{E}_{i,j+1,k+1} + \alpha\beta\chi\mathbf{E}_{i+1,j+1,k+1}.
\end{aligned} \tag{2.20}$$

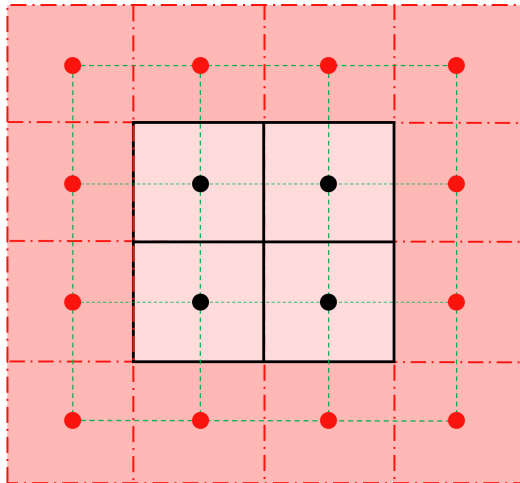


Figure 3: Virtual grids in the charge allocation. The black grids and nodes represent the real computational region, while the red dashed grids and nodes are in the virtual one. The linked green dashed grids are used for regular 2-D charge interpolation as in Figure 2. During this process, only the charge densities on the black nodes will be computed and saved.

The dimensionless parameters in Eq. (2.20) correspond to those in Eq. (2.17), thus allowing for the computation of the magnetic field \mathbf{B} on the particle through the same method. It is worth noting that the number of adjacent nodes involved in driving the particle follows the same rule as particle interpolation, and the EM fields outside the computational region are not calculated. Thus, once the particles pass through the computational boundary, the forces acting upon them are no longer considered, and they do not return to the computational region. As we do not solve the charge conservation equation, we can exclude their contribution to the source without resulting in undesired charge deposition.

2.4 GPU Implementation

According to sections 2.1 to 2.3, JefiPIC needs three major CUDA kernels, each taking over of the Jefimenko's equation, particle motion, and the charge and field interpolation, respectively.

The first CUDA kernel is designed to perform the summations presented in Eqs. (2.4) to (2.6) on GPU. Since the EM fields of a grid are produced by all \mathbf{J} and ρ in the computational region with retarded time t_r , we need to figure out the quantity of sources that should be saved. Here is our solution. Firstly, we calculate the maximum length (L_{\max}) across the computational region, while the value of L_{\max} is typically determined by the diagonal length of the computational region. We then divide L_{\max} by cdt to obtain $N_{dt} = \text{Celing}(L_{\max}/(cdt))$, which represents the maximum number of time steps an EM field travelling across the entire computational region. Consequently, the sources \mathbf{J} and ρ for at least the most recent N_{dt} time steps need to be stored to guarantee the EM field computation. For instance, at time t_A , we need to save \mathbf{J} and ρ at all grids (the

number of grids is M) for N_{dt} time steps, i.e.,

$$\begin{aligned} t_A - dt: & [\rho(r_1, t_A - dt), J(r_1, t_A - dt)], \dots, [\rho(r_M, t_A - dt), J(r_M, t_A - dt)], \\ t_A - 2 \cdot dt: & [\rho(r_1, t_A - 2 \cdot dt), J(r_1, t_A - 2 \cdot dt)], \dots, [\rho(r_M, t_A - 2 \cdot dt), J(r_M, t_A - 2 \cdot dt)], \\ & \dots\dots \\ t_A - N_{dt} \cdot dt: & [\rho(r_1, t_A - N_{dt} \cdot dt), J(r_1, t_A - N_{dt} \cdot dt)], \dots, [\rho(r_M, t_A - N_{dt} \cdot dt), J(r_M, t_A - N_{dt} \cdot dt)]. \end{aligned}$$

For time steps N that are ahead of the initial time t_0 ($t_A - N \cdot dt < t_0$), \mathbf{J} and ρ are simply set to zero. Here \mathbf{J} and ρ are cached in the global GPU memory. Obviously, this procedure requires a large amount of memory space on GPU. In practice, we limit N_{dt} to 10000, i.e., $N_{dt} = \min(N_{dt}, 10000)$, making the data storage achievable for most GPU apparatus.

Though we use a truncation level of 10000 to account for the time history, N_{dt} is frequently much smaller than it. Hence, with this approach, almost all sources can be stored in the GPU to compute the fields, thus ensuring the conservation properties in most scenarios. The cases where the value of L_{\max} by $c \cdot dt$ exceeds 10000 generally correspond to unrealistic scenarios with very large computational regions or very small time steps. For the former, the influence of distant fields on the observation point would be minimal. For the latter, it negates the advantage of JefiPIC, which is the ability to use larger time steps. Even if the truncation of integral time may introduce minor charge conservation error, this error will not accumulate owing to the integral method.

In the implementation of the integral, each thread in the CUDA kernel calculates the EM fields corresponding to a certain grid. Thus, we loop through each grid in the computational region. For convenience, we denote the i -th CUDA thread as *thread_i*, which calculates the EM fields on the i -th grid with index *grid_i*. To evaluate the EM fields of *grid_i*, we loop through all the grids to compute the Jefimenko's equation through the local sources \mathbf{J} and ρ with retarded time t_r (except for *grid_i* itself to prevent numerical divergence) and sum all the EM fields. This procedure is depicted in Figure 4.

The integrative form with a record of N_{dt} moments is beneficial for managing low-frequency electromagnetic effects. This approach sets our method apart from the quasi-static Darwin model, which presumes instantaneous transmission of information, thereby eliminating any time delay. Consequently, our proposed solver transcends the constraints of low-frequency situations as an electromagnetic solver. Nonetheless, to thoroughly account for the characteristics of electromagnetic wave propagation, it is still necessary to track the historical data while using integration methods. Furthermore, our method necessitates a mesh to carry out the integrals required to determine the charge densities defined on the mesh. This approach differs from the mesh-free method [7], where the electromagnetic fields, impacting a specific macro-particle, are ascertained by a weighted summation of other particles rather than the charge densities on the grid. Moreover, the integral equation employed in our study is entirely based on the retarded potential approach, therefore is different from the integral method of convolution operators, a stabilized version of the finite difference method. For instance, the work carried out by Wolf and his colleagues [10] presents a new integral method that eradicates the CFL restriction and does not necessitate the tracking of historical data.

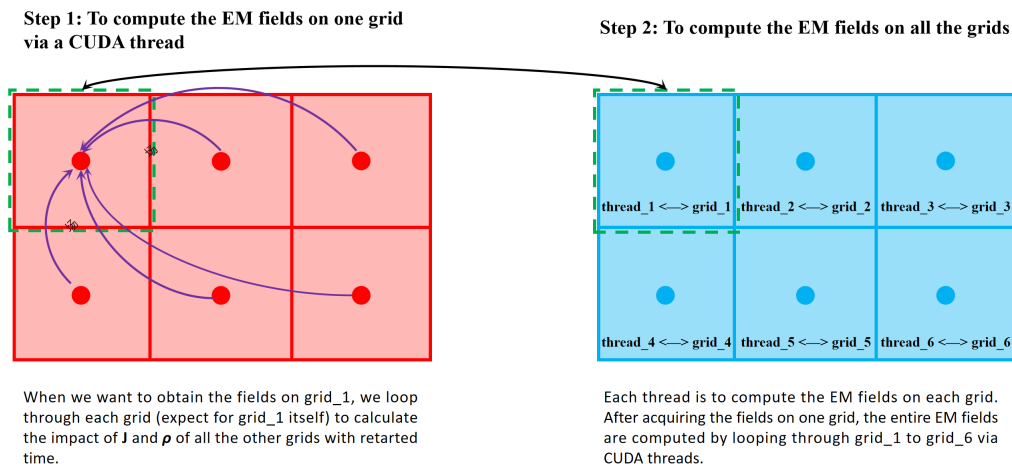


Figure 4: Process of the implementation of solving Jefimenko's equations on GPU. Supposing that the computational region contains 6 grids, and the process involves two steps. In the first step, EM fields on one grid (for example $grid_i$) are computed by looping through the other grids with \mathbf{J} and ρ . In the second step, the entire EM fields are computed by looping through the rest grids repeating the operation in step 1.

The second CUDA kernel is to achieve the particle motion exhibited by Eqs. (2.7) to (2.10). Here, the particle's displacements for full time steps and velocities for half time steps, i.e., r^n , $v^{n-1/2}$, are saved in the global GPU memory. The information update of each particle is also handled by an individual thread in the CUDA kernel. Hence, the maximum particle numbers allowed in our code is restricted by the maximum size of each dimension of a grid of thread blocks (one can simply understand it as the maximum number of threads). For one NVIDIA A100 card, this number is about 10^9 , meaning that we cannot calculate more than 10^9 particles on one GPU card.

Since \mathbf{J} , ρ , \mathbf{E} and \mathbf{B} are defined at the grid center node, we need to build the third CUDA kernel to calculate the forces on the particles and the charge and current densities on all the grid centers. To obtain \mathbf{E} and \mathbf{B} , we first iterate through all the particles in the computational region to compute \mathbf{J} and ρ for each grid. We then use the known \mathbf{J} and ρ with a retarded time to calculate \mathbf{E} and \mathbf{B} by iterating through all the grids. Here, \mathbf{J} , ρ , \mathbf{E} and \mathbf{B} are cached in the global GPU memory and all intermediate variables like α and β are set temporary local variables.

For plasma systems at different length scales, the numerical value of physical quantities can vary significantly. Given that the numerical values in JefiPIC must lie within the range of machine precision (float64), we must convert these quantities from SI unit system to a new unit system. In this paper, we use the Flexible Unit (FU) system (a brief introduction of FU is presented in the appendix), with which our code can simulate plasma systems at different length scales on GPU. By assigning proper values for constants such as vacuum permittivity ϵ_0 , reduced Planck constant \hbar , speed of light c , and λ (which relates the energy in SI and FU), we can limit most of the numerical values to machine precision. Note that the use of FU does not change the physics of the plasma system.

3 Computational Model and Results

To exhibit the comprehensive capabilities of JefiPIC, we performed a comparative study of three plasma models against three other 3-D codes. We simulated three non-neutral electron plasma models, including a) electrons emitted from a point to verify the correctness of the particle and field cut-off boundaries, b) electrons emitted with zero initial velocity to demonstrate the ease to handle non-neutral plasma, and c) electrons emitted with random initial velocity, showcasing the natural charge conservation feature. The alternative codes we used include UNIPIC, a mature PIC code, EPOCH, an open-source PIC code, and RGB-Maxwell, a plasma simulator. UNIPIC and EPOCH are traditional FDTD-based PIC codes, while RGB-Maxwell solves the Boltzmann equations. Here, we list some presets of these codes.

Particle boundary condition — The three PIC codes all use the cut-off boundary to 'kill' the particles that leave the computational region, and RGB-Maxwell directly estimate the particle distribution function outside the computational region.

Field boundary condition — Codes based on difference method utilize convolutional perfect matched layers (CPML) as the field boundary [43]- [44], while those based on integral method use a simple cut-off boundary.

Space grid and time step — All four codes divide the computational region with the same spatial grid size of $dx = dy = dz = 10^{-5}$ m. The total computational time is set to 1 ns. UNIPIC and EPOCH use the difference methods, thus requiring the time step dt to at least satisfy the CFL condition,

$$c \cdot dt \leq \frac{1}{\sqrt{\frac{1}{(dx)^2} + \frac{1}{(dy)^2} + \frac{1}{(dz)^2}}}, \quad (3.1)$$

limiting dt to no more than around 1.92×10^{-14} s. JefiPIC and RGB-Maxwell utilize Jefimenko's equations instead, which are not limited by numerical stability. Therefore, we set the time step as $dt = 10^{-13}$ s, which is five times larger than that used in difference methods.

Particle — To efficiently achieve the computation, we used macro-particle to represent electrons in the similar phase space. The ways to handle macro-particles are different in different codes. JefiPIC implements individual tracking for all macro-particles using CUDA kernels on an NVIDIA A100 GPU card, which has a maximum limit of around 10^9 CUDA threads. Therefore, we are limited to running simulations with a maximum of 10^9 particles at once. To reduce the numerical and statistic noise, we use 10^7 particles in the JefiPIC simulation. EPOCH can automatically merge and split the weights of the particles ensuring an approximate count of 100 particles in each grid to keep the statistical error during the simulation. In UNIPIC, a fixed particle weight leading to at least 10^5 particles is set to balance numerical noise and execution time before the simulation. On the other hand, RGB-Maxwell use a distribution function on a six-dimensional phase space instead of the concept of 'particle'. The initial velocity is represented in the units of m/s in our simulation, and the energy corresponding to the velocities v_0 used in the following experiments equals to 10 eV.

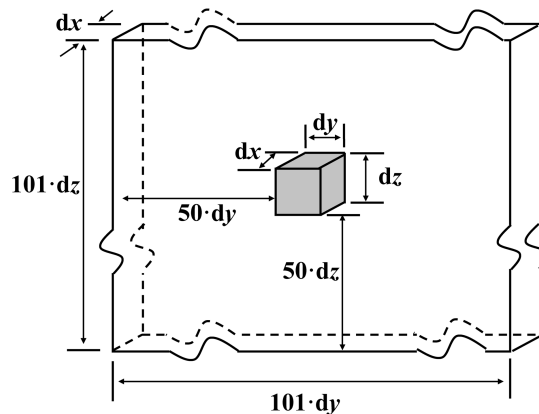


Figure 5: Initial particle distribution. The computational region was of size $1 \cdot dx \times 101 \cdot dy \times 101 \cdot dz$ in JefiPIC and RGB-Maxwell. The particles are placed in the shaded region uniformly in the cuboid volume of $1 \cdot dx \times 1 \cdot dy \times 1 \cdot dz$ ranging from $50 \cdot dy$ to $51 \cdot dy$ in the y -axis and $50 \cdot dz$ to $51 \cdot dz$ in the z -axis. The velocities of the particles obey the Gaussian distribution in the yoz plane.

Note that: Though JefiPIC is able to handle 3D projects, we execute 2D-like or 1D problems in our following simulations for the better comprehension and explanation of JefiPIC.

3.1 Perfect Absorbing Layer

The boundary of PIC contains two components: the field boundary and particle boundary. In the difference-based PIC, the accuracy of the EM fields is highly sensitive to the choice of field boundary layers, and simple methods for 'kill' particles in the boundary layer can introduce undesirable electrostatic field errors. JefiPIC, on the other hand, effectively handles the absorption of fields and particles at the computational boundary with a simple cut-off boundary, aided by the integral operation. A comparative simulation has been conducted between JefiPIC and RGB-Maxwell.

In the two integral PIC code, the total charge of electrons is of -5×10^{-14} C. They are emitted in all directions in the yoz plane from a central point ($i=1, j=50, k=50$), initialized with a Gaussian distribution of velocities with an average velocity of v_0 and a standard deviation of $0.2v_0$. This model is simulated by JefiPIC and compared to RGB-Maxwell with the computational region size as $nx \cdot ny \cdot nz = 1 \times 101 \times 101$ shown in Figure 5.

Figure 6 depicts the particle distribution of the two models at different time instances. The top row displays the results from the particle model, while the bottom row shows those from the distribution function. The figure demonstrates that the two particle distributions are nearly identical, with most of the particles forming a prominent light ring that spreads out gradually over time. This outcome confirms the general results obtained from JefiPIC. Moreover, since the integral method naturally filters out particles that are outside the computational domain, no charge deposition occurs when the particles pass through the computational boundary, and any electromagnetic force on those escape

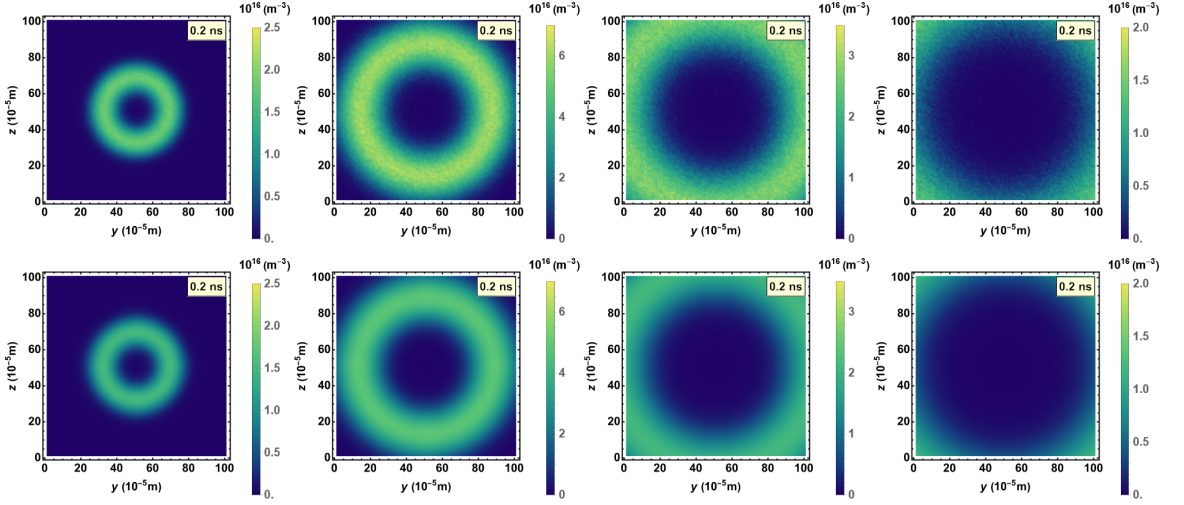


Figure 6: Particle distributions over time. Panel (a) shows the distribution at 0.2 ns, followed by (b) at 0.4 ns, (c) at 0.6 ns, and (d) at 0.8 ns. The two rows represent the particle distributions obtained from JefiPIC and RGB-Maxwell, respectively.

particles would not be taken into account. Consequently, the motion of the particles is not hindered, and the ring-like particle distribution is sustained.

In Figure 7, the electric fields of the two models are plotted at grid $(i=1, j=75, k=75)$, which is $25 \cdot dx$ and $25 \cdot dy$ distant from the particle emission point. As particles spread towards the diagnostic point, the electric field initially becomes negative and then transitions to positive before gradually decreasing towards zero as most of the particles pass and move away from the diagnostic point. The electric fields in both models display similar waveforms that are smooth with no observable reflections, suggesting that the electric field does not interfere with the particle distribution.

Through Figure 6 and Figure 7, we can observe that despite utilizing the first-order charge and field interpolation method, JefiPIC delivers results as accurate as those obtained from the second-order accurate plasma simulator RGB-Maxwell.

As a result, the integral-based PIC method JefiPIC is capable of naturally cutting off fields and particles at the computational boundary without reflecting the fields or causing charge deposition errors. This makes JefiPIC a more effective approach compared to the difference-based PIC methods that rely on boundary conditions. Thus, JefiPIC is particularly well-suited for modeling open-boundary problems, such as space plasma [48], quark-gluon plasma [45], or high-altitude nuclear explosions [49]- [51].

3.2 Electrostatic effect

3.2.1 Non-neutral plasma

As previously mentioned, the integral-based PIC method has the advantage of its ability to handle non-neutral plasma without Poisson pre-processing. Here, we compare the evolution of a batch of electrons with zero velocity in JefiPIC, EPOCH, and RGB-Maxwell.

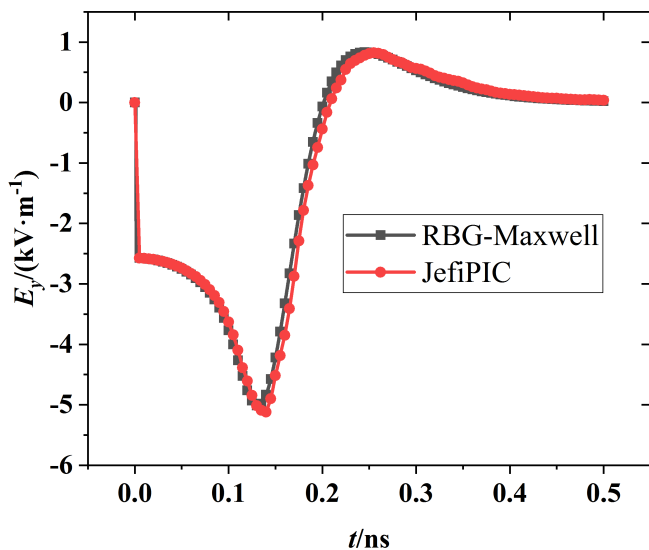


Figure 7: Comparison of y -direction electric field. The y -direction electric fields at point $(i=1, j=75, k=75)$ derived from JefiPIC and RGB-Maxwell are compared. The black square and red circle represent the results from RGB-Maxwell and JefiPIC.

The total charge of electrons is -5×10^{-14} C. We select the computational region size as $n_x \cdot n_y \cdot n_z = 1 \times 251 \times 111$ in JefiPIC and RGB-Maxwell, and $n_x \cdot n_y \cdot n_z = 3 \times 251 \times 111$ in EPOCH. Initially, these electrons are placed uniformly within a cuboid region of size $1 \cdot dx \times 1 \cdot dy \times 101 \cdot dz$, ranging from $0 \cdot dx$ to $1 \cdot dx$ ($1 \cdot dx$ to $2 \cdot dx$ in EPOCH) in the x -axis, $124 \cdot dy$ to $125 \cdot dy$ in the y -axis and $5 \cdot dz$ to $106 \cdot dz$ in the z -axis, shown in Figure 8. To better observe the evolution of particles, we apply a constant magnetic field of 10 T along the y -direction to constrain the electrons' transverse motion, considering velocity only in the y -direction.

Due to the mutual repulsion between particles, it is expected that they should diffuse from the center to both sides along y -axis. As depicted in Figure 9, particles simulated by JefiPIC and RGB-Maxwell consistently spread out as expected. However, EPOCH fails to demonstrate a reasonable distribution when pre-processing tasks, such as Poisson's equation, are not executed correctly. This outcome can be explained by the fact that JefiPIC and RGB-Maxwell utilize Jefimenko's equations, which can model the EM field as long as charge and current densities are supplied. Therefore, even in the absence of initial current, the electrostatic fields calculated from the charge density can still drive the charges apart. In contrast, EPOCH is a current-based PIC code. To achieve the same result, we must perform the pre-processing to offer the equivalent electrostatic fields, such as solving the Poisson's equation. However, this essential operation will lead to additional computation time.

To further validate the accuracy of JefiPIC, we compare its particle number density distribution with the analytical solution [52],

$$\psi \sim \frac{1}{\tau [y^2/2\tau^2 + 1/\psi_0]'} \quad (3.2)$$

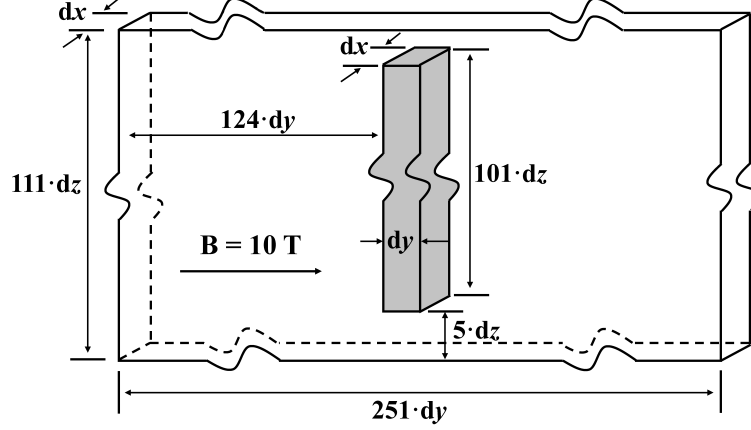


Figure 8: Initial particle distribution. The computational region was of size $1 \cdot dx \times 251 \cdot dy \times 111 \cdot dz$ in JefiPIC and RGB-Maxwell, and of size $3 \cdot dx \times 251 \cdot dy \times 111 \cdot dz$ in EPOCH. The particles are placed in the shaded region uniformly in the cuboid volume of $1 \cdot dx \times 1 \cdot dy \times 101 \cdot dz$ ranging from $0 \cdot dx$ to $1 \cdot dx$ ($1 \cdot dx$ to $2 \cdot dx$ in EPOCH) in the x -axis, $124 \cdot dy$ to $125 \cdot dy$ in the y -axis and $5 \cdot dz$ to $106 \cdot dz$ in the z -axis. The velocities of the particles are zero.

where ψ , τ , and y represent the normalized number density, time and distance. As illustrated in Figure 10, the particle distributions produced by JefiPIC closely match the analytical solution.

Constrained by the requirement to adopt non-absorbing boundary conditions when solving Poisson equations, the available open-source PIC codes with built-in Poisson solvers may inadvertently generate undesired reflected fields, which could consequently alter the motion of the particles

3.2.2 Two stream instability

Applied with period boundary condition according to Ref. [55], we simulate the 1-D two stream instability with two counter-streaming electron beams with initial energy of $E_0 = 1\text{eV}$ along y axis. The two electron beams consisting of total charge -5×10^{-14} C are emitted into a static uniform neutralizing background charge. We take $L_y = 3 \times 10^{-4}$ m and $k = 2\pi/L_y$, the computational time $t = 2\text{ns}$ and the time step $dt = 4 \times 10^{-4}$ ns. According to the dispersion relation for the two stream instability from Ref. [54], we have

$$D(\omega, k) = 1 - \omega_p^2 \left[\frac{1}{(\omega - ku)^2} + \frac{1}{(\omega + ku)^2} \right] \quad (3.3)$$

which gives the greatest growth rate of $\gamma = 0.0935$, where ω_p is the plasma frequency, and u is the relativistic velocity of particle. The growth of this mode of electric field (black

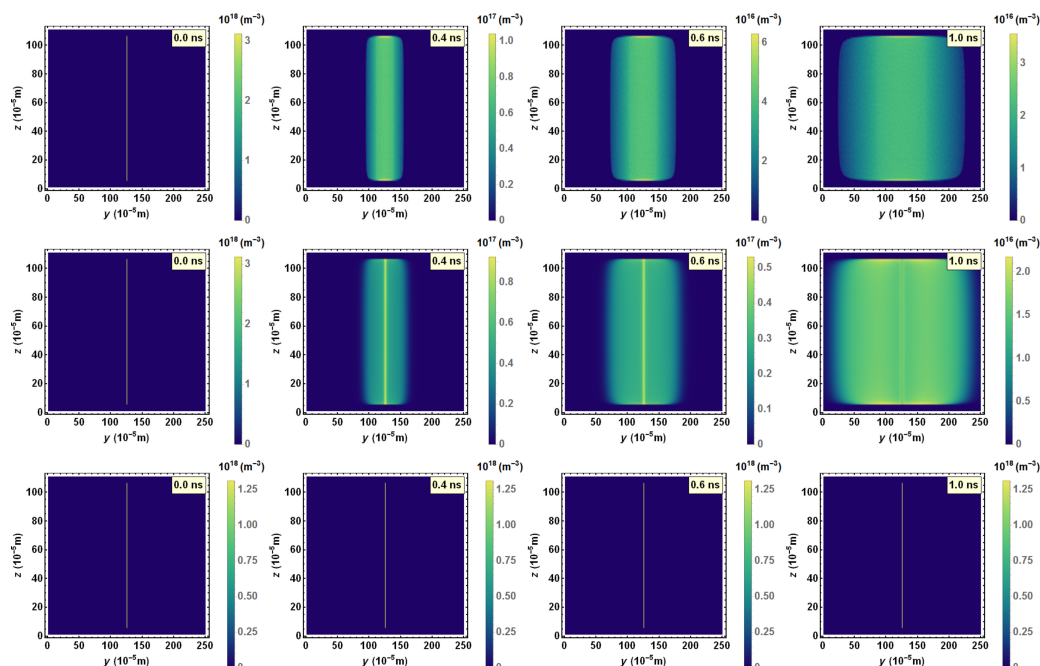


Figure 9: Particle distributions over time. The three rows represent the particle distributions obtained from JefiPIC, RGB-Maxwell, and EPOCH, respectively. Panel (a) shows the distribution at 0.0 ns, followed by (b) at 0.4 ns, (c) at 0.6 ns, and (d) at 1.0 ns.

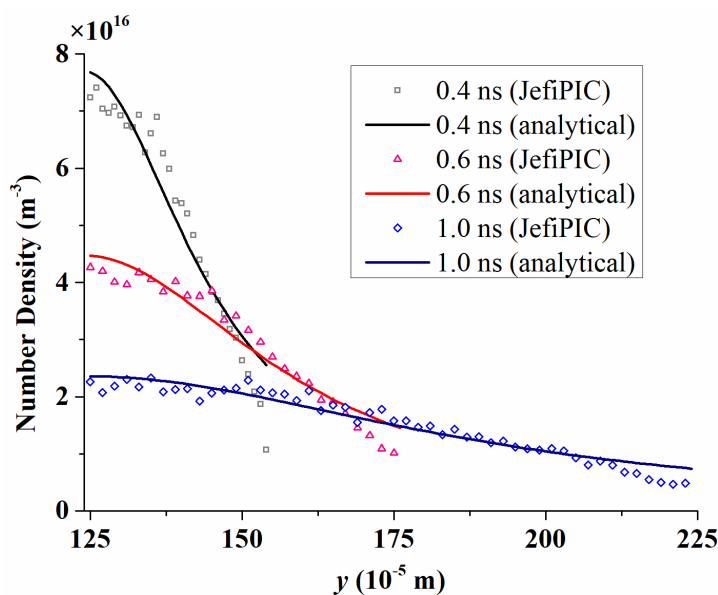


Figure 10: Simulated and analytical particle number density distribution. The figure displays the simulated particle number density distribution obtained through JefiPIC and the analytical solution from Reference [52] at $t=0.4$ ns, 0.6 ns, and 1.0 ns. The data are extracted from the grids ranging from $[0 \text{ dx to } 1 \text{ dx}, 125 \text{ dy to } 225 \text{ dy}, 54 \text{ dz to } 55 \text{ dz}]$. The gray hollow square, pink hollow triangle and blue hollow rhombus represent the results by JefiPIC, while the black, red, and dark blue lines represent the analytical results.

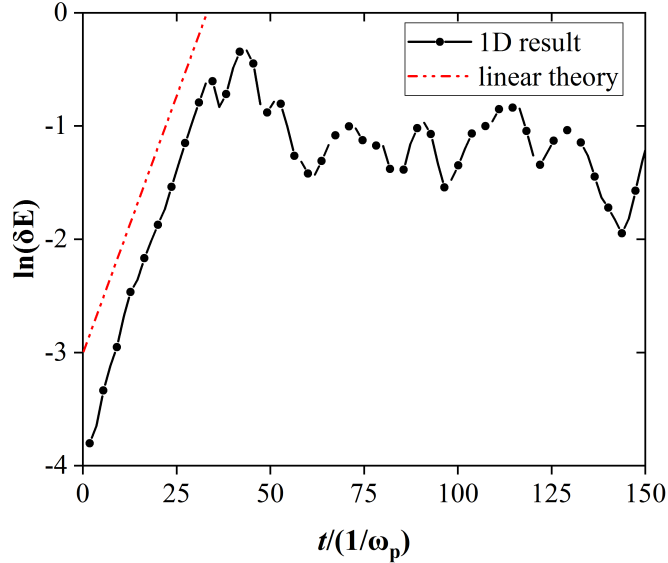


Figure 11: Growth of the mode with growth rate in the two stream instability. The black line represents the 1D numerical results, and the red line is the prediction of linear theory, which are consistent with each other. We set $L_y = 3 \times 10^{-4}$, $k = 2\pi/L_y$ and $\gamma = 0.0935$.

line) is shown in Figure 11, and agrees well with the rate from linear theory (red line). We also plot the phase space distribution in Figure 12, and the two separate distribution lines “roll up” obviously after the interaction of beams.

3.3 Obeying Charge Conservation Law

Charge conservation is indeed critical in PIC simulation. The linear weightings for current may not satisfy the continuity equation in the finite difference method. This is because the finite difference-based PIC method implicitly computes electric field solely through electric current. Although theoretically, as long as current continuity is established, the conservation property is preserved, the linear current interpolation method based on the finite difference method can potentially violate the conservation law, thus causing the electric field divergence equation to fail. However, by utilizing Jefimenko’s equation, a Green’s function-like formulation, the electric field is explicitly computed by the actual sources - i.e., all the charge density, time-varying charge density, and current density, and integrated across the entire computational region. This integration method can circumvent the charge conservation problem.

3.3.1 Verification of charge conservation law

We employ JefiPIC to simulate the beam expansion problem proposed in Ref. [53] to verify the charge conservation law. Electrons with initial energy of 30 keV and a current of 5 A are injected from the left boundary into the space and are removed from the simulation as long as they arrive the right boundary. The simulation space adopts the absorbing field and particle boundary condition. Figure 13 shows the particle distributions

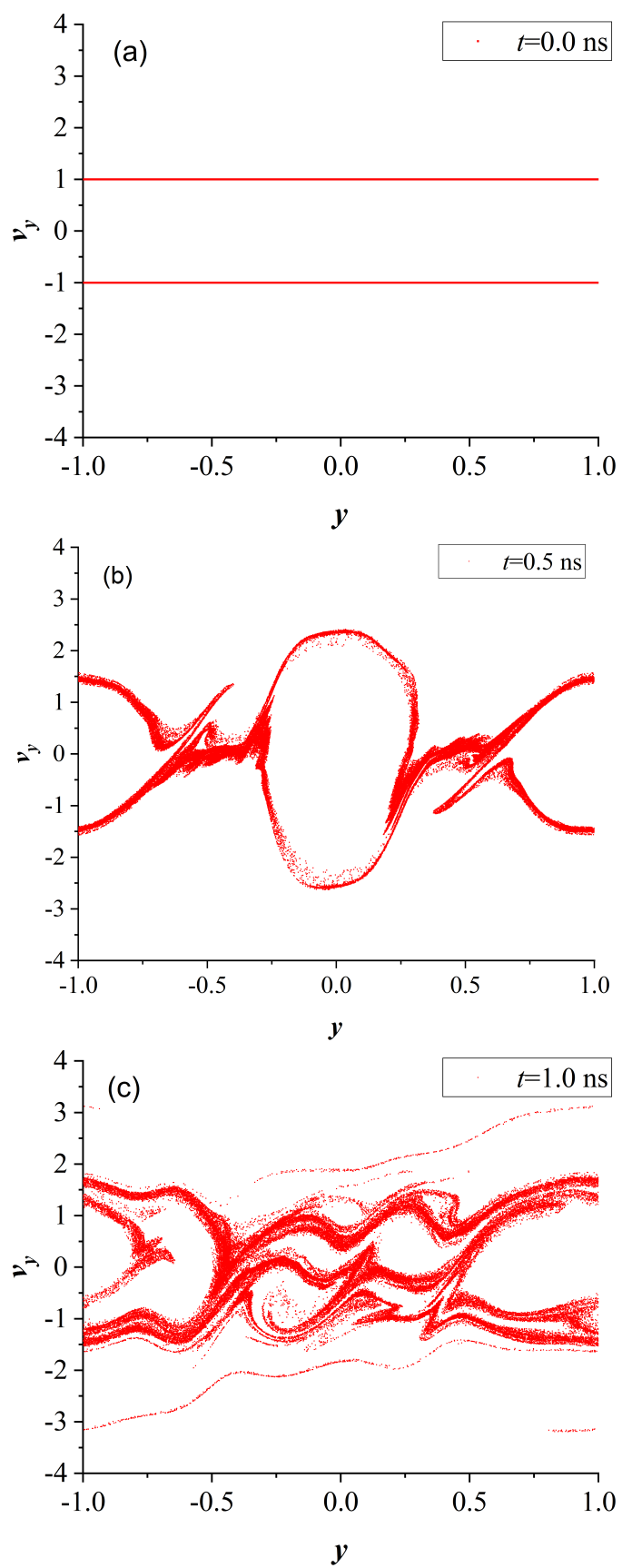


Figure 12: Particle phase space plots for the 1D two stream instability problem. (a) $t=0.0ns$, (b) $t=0.5ns$, (c) $t=1.0ns$. The initial velocities and displacements are normalized.

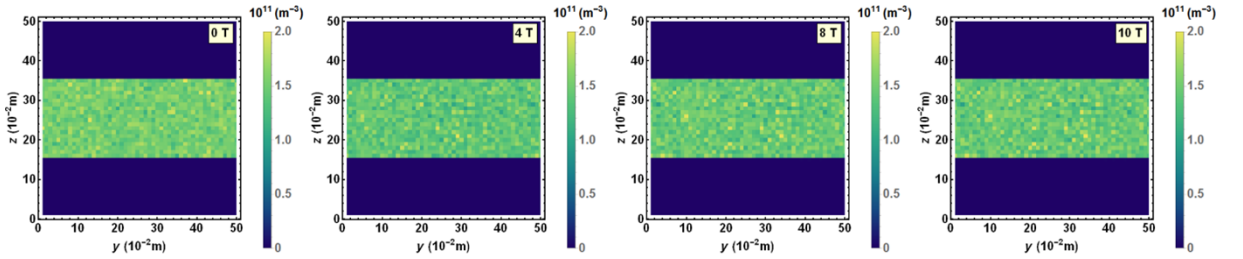


Figure 13: Beam distribution at different time shots. T represents the electron transit period for electron initial energy of 30 keV and the transit distance long y axis of 1 m.

Table 1: Comparison of the maximum particle displacement and velocity between JefiPIC and UNIPIC

Time/ns	Maximum Displacement/m		Maximum Velocity/(m s-1)	
	JefiPIC	UNIPIC	JefiPIC	UNIPIC
0.4	8.43×10^{-4}	8.49×10^{-4}	2.20×10^6	2.26×10^6
0.6	1.29×10^{-3}	1.30×10^{-3}	2.25×10^6	2.30×10^6

simulated by our PIC code which only uses a simple bilinear current weighting without using a divergence correction. The result shows that the beam spreads transversely only slightly as it traverses the system due to its space charge force during the simulation up to 10 transit period.

3.3.2 Compared with UNIPIC

We choose another FDTD-based PIC code, UNIPIC, to further demonstrate the advantage of the integral-based PIC codes when dealing with the charge-conservation problem. Since UNIPIC obeys the charge-conservation law that when electrons are emitted from the shaded rectangle face, the pseudo positive charge with the opposite charge will retain at the emission surface. The total charge of electrons is -5×10^{-14} C. The electrons' initial velocities in the y -direction are randomly from 0 to v_0 . We select the computational region size as $n_x \cdot n_y \cdot n_z = 1 \times 251 \times 111$ in JefiPIC, and $n_x \cdot n_y \cdot n_z = 3 \times 251 \times 111$ in UNIPIC. We apply a constant magnetic field of 10 T in the y -direction again to constrain the electrons' transverse motion, shown in Figure 14. Thus, only velocities in the y -direction are considered.

Note that: UNIPIC employs the simple linear interpolation method rather than the strict charge-conservation method, and thus it needs to use the Langdon-Marder correction algorithm at a certain frequency.

Figure 15 displays the particle distribution obtained from JefiPIC and UNIPIC at two different times. A comparison of the two distributions reveals their overall similarity, validating our code's results to a certain extent. Table 2 lists the maximum displacement and velocity of particles under corresponding time steps in Figure 15. It is shown that the particles states simulated by JefiPIC and UNIPIC are in close agreement, with deviation around $1 \sim 3\%$.

Figure 16 exhibits the y -direction electric fields at point ($i=0, j=50, k=55$) in JefiPIC

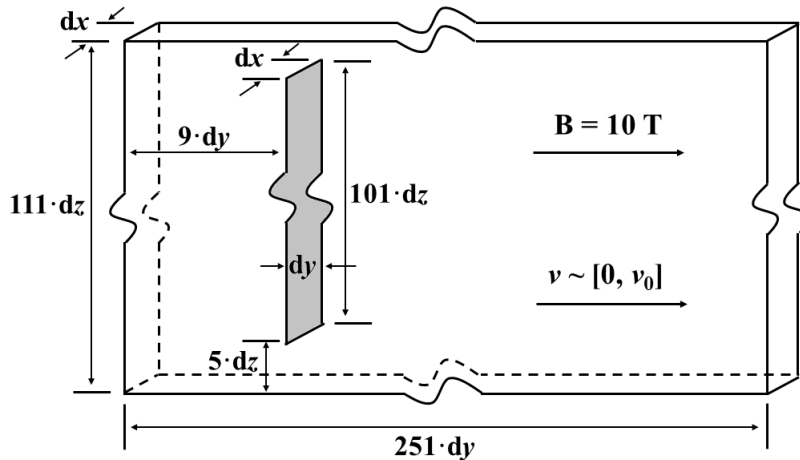


Figure 14: Initial electron distribution in the simulation. The total computational region was of size $1 \text{ dx} \times 251 \text{ dy} \times 111 \text{ dz}$ in JefiPIC and $3 \text{ dx} \times 251 \text{ dy} \times 111 \text{ dz}$ in UNIPIC. The particles were placed uniformly on the shaded rectangle face of $y=9 \cdot \text{dy}$ and $1 \text{ dx} \times 101 \text{ dz}$, with 0 dx to 1 dx (1 dx to 2 dx in UNIPIC) in the x -axis and 5 dz to 106 dz in the z -axis. Particle velocities obeyed a random distribution from 0 to v_0 .

and at point $(i=1, j=50, k=55)$ in UNIPIC for detail. The electric fields of the two simulations match with each other in the respect of peak value and peak time, but differ in two aspects: a) the pulse width of JefiPIC's field is larger, and b) JefiPIC's trailing edge field changes to positive due to the charge separation. Besides, JefiPIC shows a significantly smoother electric field profile in comparison to UNIPIC.

Thus, in the aspect of charge conservation, the integral method provides a natural advantage in terms of accuracy and simplicity over the difference method in PIC, despite the fact that the difference-PIC has already incorporated the necessary Langdon-Marder amendment algorithms.

We also compared the computational performance of the two codes. UNIPIC was run on a workstation with Intel Xeon Processor E5-2650 v4 CPU across 200 threads, and it took over 6 hours to complete the calculations. In contrast, using a larger time step, JefiPIC completed the computations within only half an hour on a single GPU A100 card, achieving over 90% time-saving benefits.

3.4 Choice of Macro-Particle, Grid number, Time step and N_{dt}

We conduct test on JefiPIC's time consumption with varying macro-particle numbers and grid numbers to provide readers with additional reference. It can be concluded from Figure 17 (a) that when the particle number is less than one percent of the CUDA kernel limitation (\sim just under 10^7), the computational time keeps relatively short due to the high degree of parallelism on GPU and a small number of data transfer between CPU and GPU. However, once the particle number exceeds 10^7 , the time cost increase significantly. Note that the particle number in JefiPIC (i.e., the occupied kernel number) must not

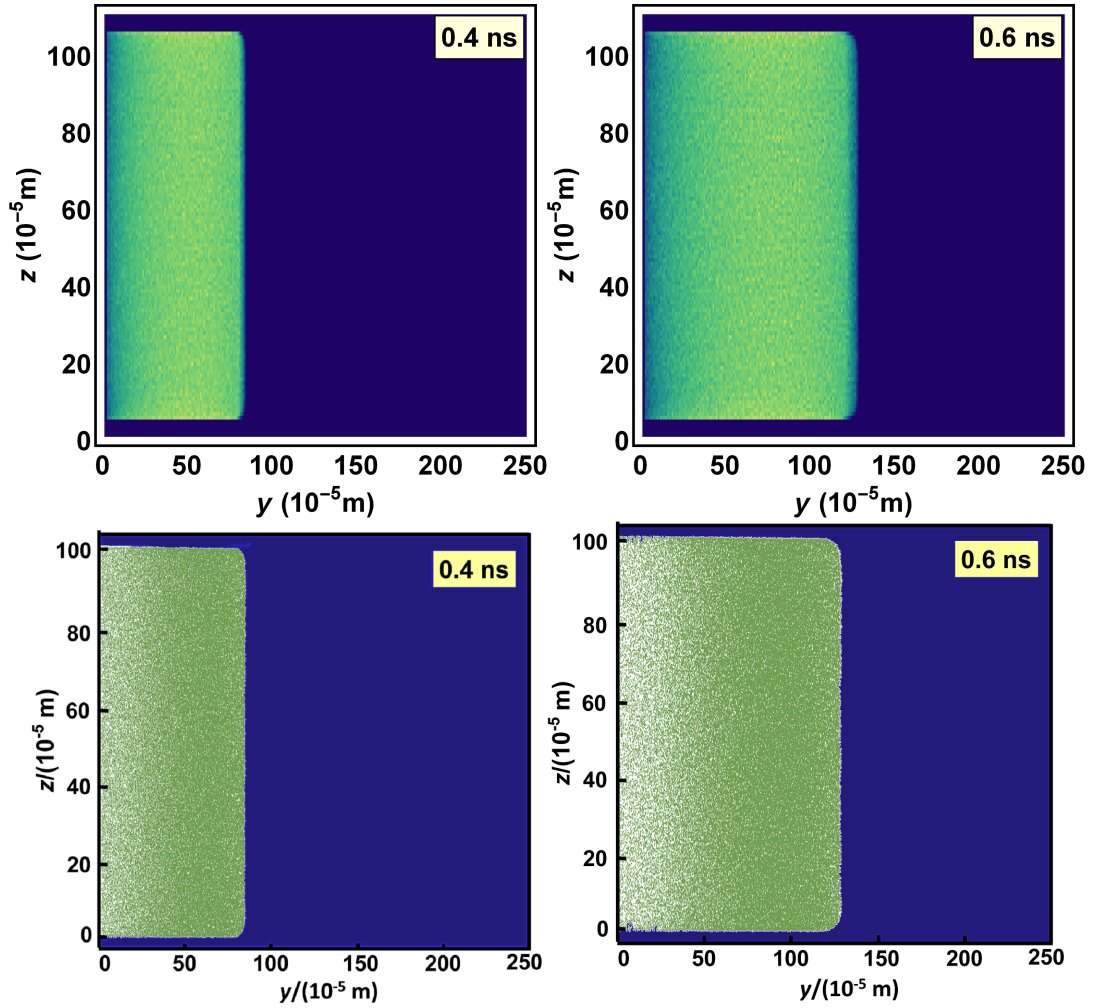


Figure 15: Comparison of particle distributions at $t = 0.4$ ns and $t = 0.6$ ns in (a) JefiPIC and (b) UNIPIC simulations. Initial velocities were applied only in the y -direction, randomly ranging from 0 to v_0 . This illustrates the differences in Coulomb forces between the two simulations, highlighting the more accuracy of JefiPIC in simulating particle movements.

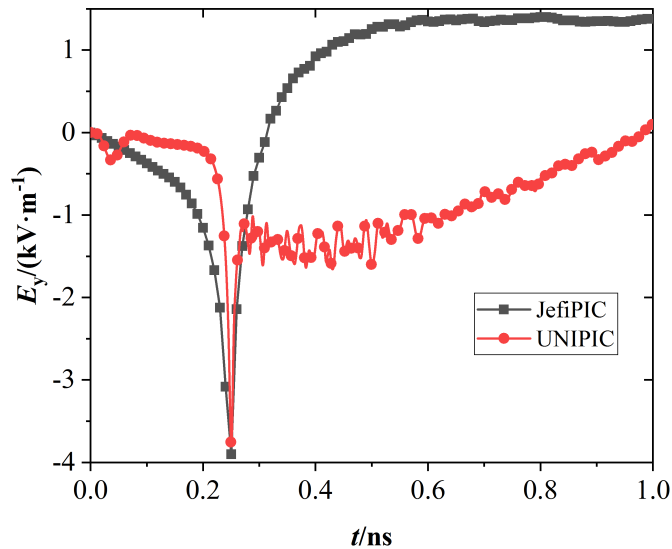


Figure 16: Comparison of y -direction electric field. The y -direction electric fields at point $(i=0, j=50, k=55)$ derived from JefiPIC and at point $(i=1, j=50, k=55)$ from UNIPIC are compared. The black square and red circle represent the results from JefiPIC and UNIPIC.

exceed the CUDA limitation (10^9), or the computation will fail. Fortunately, $10^7 \sim 10^8$ macro-particles are typically sufficient for most simulations within the controlled noises.

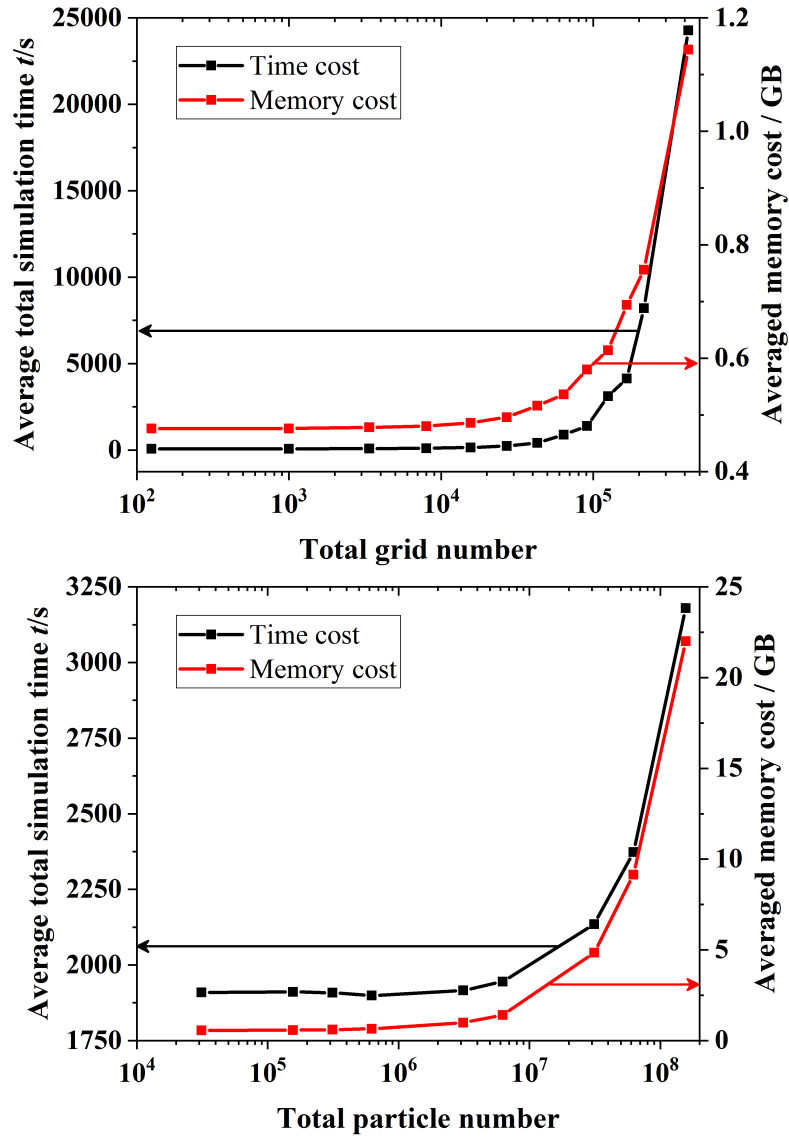
Besides, the FLOPS of the A100 card is approximately 312 TFLOPS, and the efficiency of our code on A100 exceeds 99%, implying that the FLOPS of JefiPIC is also around 312 TFLOPS on A100. We count the computational time the three main kernels cost, shown in Table 2. The results indicate that the interpolation process occupies the majority of computational time (around over 95%), and that total I/O operations require approximately 60 seconds, which is relatively negligible when compared to the extensive computational time executing the CUDA kernel functions. Increasing the number of grids will extend interpolation time, while augmenting the number of particles will increase particle motion time.

As for the grid number exhibited in Figure 17 (b), the similar tendency can be observed. In the grid range we compute, though the GPU memory cost increase only no more than three times with the increase of grid number, the time cost increase over 4000 times when the grid number exceeds around 10^5 , while on the contrary the increase rate of memory cost is larger for the increase of macro-particle. We find that JefiPIC is able to solve a project with maximum of 10^7 grid on one GPU card limited by the GPU memory (40GB). However, the above condition is not achievable since the time cost is far too large.

Since we mentioned before that JefiPIC is not sensitive to the choice of time step when computing the EM field, we compare the electric field in the model of the circle expansion model in section 3.1. In this model, though the time step varies from the CFL-limited time step (2×10^{-14} s) to its 250 times (5×10^{-12} s), the electric field changes little, as shown in Figure 18. We can conclude that the JefiPIC indeed has the advantages of the

Table 2: Comparison of the maximum particle displacement and velocity between JefiPIC and UNIPIC

Grid Size	Particle Number	Time cost/s (Proportion)		
		EM solver	Interpolation	Particle motion
1×251×111	4.16×10^4	3.77 (1.05%)	476.74 (98.32%)	1.17 (0.63%)
	4.16×10^6	4.96 (0.78%)	465.75 (98.97%)	3.01 (0.25%)
1×101×101	4.16×10^4	3.74 (2.54%)	142.39 (96.68%)	1.16 (0.78%)
	4.16×10^6	5.64 (3.81%)	139.31 (94.25%)	2.86 (1.94%)

Figure 17: Time cost of JefiPIC with varying particle numbers. The maximum CUDA threads limits the maximum number of particles to 10^9 .

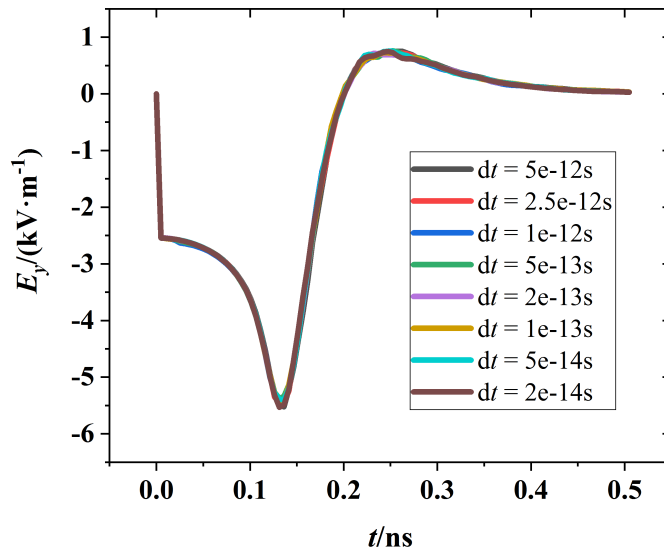


Figure 18: Electric fields with different time steps from CFL-limited time step (2×10^{-14} s) to its 250 times (5×10^{-12} s).

flexibility of the choice of time step.

Note that: The time step should also be limited by resolving the plasma period obtained according to the plasma density.

Last, we report the influence of the parameter N_{dt} . In our methodology, we indeed use a truncation level of 10000 to account for the time history. However, the actual N_{dt} required to store the sources is determined by the minimum value between 10000 and the ratio of the diagonal length of the computational region L_{\max} to the time step dt used in Jefimenko's equation. Consequently, $L_{\max}/(c dt)$ is frequently much smaller than 10000 and varies with the size of the computational region. With this approach, in most scenarios, all sources can be stored in the GPU to compute the fields, thus ensuring the conservation properties of our method. The cases where the ratio of $L_{\max}/(c dt)$ exceeds 10000 generally correspond to unrealistic scenarios with very large computational regions or very small time steps. For the former, the influence of distant fields on the observation point would be minimal. For the latter, it negates the advantage of JefiPIC, which is the ability to use larger time steps. In light of this, we have conducted an additional example where the electric current density and electric charge density are governed by analytical equations:

$$J_x = J_y = J_z = \sin(x+y+z) \cdot \sin(t) \quad (3.4)$$

$$\rho = 3(\cos(t) - 1) \cdot \cos(x+y+z) \quad (3.5)$$

The above equations naturally satisfy the continuum equation. For convenience, we set the fundamental constants c (the speed of light), ϵ_0 (vacuum permeability) and μ_0

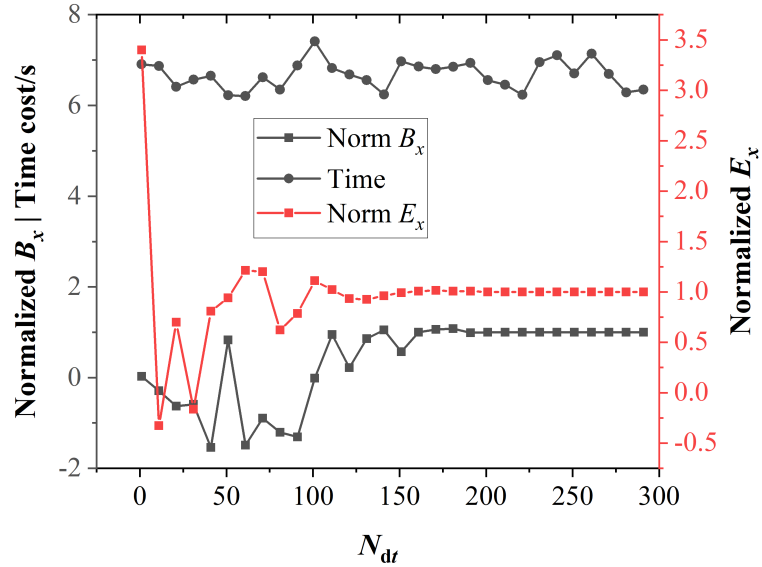


Figure 19: Normalized summation of the Magnetic Field B_x and Electric Field E_x over the entire space and variation of execution time with the change of N_{dt} .

(vacuum permittivity) to be unit 1, i.e., the Rationalized Heaviside-Lorentz Units. We choose a cubic of grid sizes $[20,20,20]$, with $[dx,dy,dz]=[0.3,0.3,0.3]$ and $dt=0.05$. In the current set-up, the maximum distance within the cubic is its diagonal, which is about $\sqrt{3 \times (20 \times 0.3)^2}$. Hence the maximum time steps required for the electromagnetic wave to transmit from one corner to another is $\sqrt{3 \times (20 \times 0.3)^2} / dt \approx 207$, which means the maximum length of the time steps tracked in the history should be larger than 207. To see this, we loop through a series of track length, i.e., $N_{dt} = [1, 11, 21, \dots, 291]$. In Figure 19, we depict the scanned results. As can be seen, the calculated electromagnetic fields display significant fluctuations when N_{dt} is approximately less than 200. In contrast, when N_{dt} is around 200 or more, the results appear to be consistent. This suggests that the value of N_{dt} could be estimated based on the maximum time steps necessary for the transmission of the electromagnetic wave from one corner to another.

4 Conclusion

This paper purposes JefiPIC, a powerful plasma simulation package that uses a 3-D particle-in-cell method in conjunction with Jefimenko's equations to accurately model plasma systems. Despite its complexity, we have successfully implemented JefiPIC on GPU for practical calculations. JefiPIC is more user-friendly and easier to get started with, as it doesn't require many complicated amendment algorithms. This makes it an alternative option for newcomers who want to dive into the field of particle-in-cell simulations.

Our comparative study between UNIPIC, EPOCH, and RGB-Maxwell has revealed

that JefiPIC has certain advantages in the following aspects. First, JefiPIC's use of integral operation enables accurately employing the linear particle-to-grid apportionment technique, which simplifies the numerical scheme and brings less noise. Secondly, JefiPIC naturally cuts off charge and field at the computational boundary, preventing field reflection or charge deposition. Third, JefiPIC does not require extra pre-processing, making it a superior choice for calculating non-neutral plasma cases. Fourth, the integral equations used in JefiPIC free the simulation from the CFL condition, enabling larger time steps and helping to conserve computational resources. Finally, the results obtained from JefiPIC are comparable to those obtained using second-order accurate Boltzmann equations. Overall, our study demonstrates that JefiPIC is a promising and time-efficient method for simulating plasma physics problems with open boundary conditions.

However, to increase JefiPIC's versatility, the next version will incorporate interactions between electrons and neutral molecules or charged ions. Also, measures will be taken to improve the efficiency of the integral operation or to accomplish the parallel computing. We believe that these improvements will extend the applicability of JefiPIC further and help advance our understanding of plasma behavior.

Acknowledgments

We express our gratitude to Prof. Jian-Guo Wang, Associate Researcher Zai-Gao Chen, and Assistant Researcher Ze-Ping Ren from NINT for their valuable contributions and insightful discussions on the PIC simulations. The work is supported by the National Key Research and Development Program of China under Grant No. 2020YFA0709800 and the National Natural Science Foundation of China (NSFC) under Grants No. 12105227.

A The unit conversion table

In Flexible Unit (FU), all physical quantities have the dimension of energy E , shown in Table 3. One needs to choose proper values for λ , c , \hbar , ϵ_0 so that all numerical quantities are in the range of float64 on GPU, where c , \hbar , ϵ_0 denote the speed of light, the reduced Planck constant, and the vacuum permittivity. λ is constant relating the energy quantity between SI and FU.

References

- [1] J. Dawson, One-dimensional plasma model, *The Physics of Fluids*, 5 (1962), 445-459.
- [2] A. B. Langdon and C. K. Birdsall, Theory of plasma simulation using finite-size particles, *The Physics of Fluids*, 13 (1970) 2115-2122.
- [3] C. K. Birdsall and D. Fuss, Clods-in-clouds, clouds-in-cells physics for many-body plasma simulation, *Journal of Computational Physics*, 3 (1969) 494-511.
- [4] B. Marder, A method for incorporating Gauss' law into electromagnetic PIC codes, *Journal of Computational Physics*, 68 (1987) 48-55.
- [5] J. Villasenor, O. Buneman, Rigorous charge conservation for local electromagnetic field solvers, *Computer Physics Communications*, 69 (1992) 306-316.

Table 3: The transform of the physical quantities from SI Unit to Flexible Unit

Physical quantity	SI Unit	Flexible Unit
Magnetic field	T	$5.01398 \times 10^{-36} / (\lambda^2 \hbar^{3/2} \epsilon_0^{1/2} c^{5/2}) E^2$
Length	m	$3.16304 \times 10^{25} \hbar c \lambda E^{-1}$
Time	s	$9.48253 \times 10^{33} \hbar \lambda E^{-1}$
Electric charge	C	$1.89032 \times 10^{18} (\hbar \epsilon_0 c) 1/2$
Momentum	$\text{kg} \cdot \text{m} \cdot \text{s}^{-1}$	$2.99792 \times 10^8 / (c \lambda) E$
Energy	J	$1 / \lambda E$
Mass	kg	$8.89752 \times 10^8 / (c^2 \lambda) E$
Electric current	A	$1.99347 \times 10^{-16} (\epsilon_0 c / \hbar)^{1/2} / \lambda E$
Electric field	$\text{V} \cdot \text{m}^{-1}$	$1.67249 \times 10^{-44} / (\lambda^2 \hbar^{3/2} \epsilon_0^{1/2} c^{3/2}) E^2$
Force	$\text{kg} \cdot \text{m} \cdot \text{s}^{-2}$	$3.16153 \times 10^{-26} / (\hbar \epsilon_0 c) E^2$
Unit charge	1	$0.30286 (\hbar \epsilon_0 c)^{1/2}$

- [6] G. Paul, and Sutmann Godehard, Long-range interactions in many-particle simulation, Quantum simulations of many-body systems: from theory to algorithm, 10 (2002) 467-506.
- [7] Siddi Lorenzo, Lapenta Giovanni and Gibbon Paul, Mesh-free Hamiltonian implementation of two dimensional Darwin model, Physics of plasmas, 24 (2017) 082103.
- [8] Andrew J. Christlieb, R. Krasny, J.P. Verboncoeur, et. al., Grid-Free plasma simulation techniques, IEEE Transactions on Plasma Science, 34 (2006) 149-165.
- [9] A.J. Christlieb, W. Hitchon, J. Lawler and G. Lister, Integral and Lagrangian simulations of particle and radiation transport in plasma, Journal of Physics D: Applied Physics, 42 (2009) 194007.
- [10] Eric M. Wolf, M. Causley, A.J. Christlieb, and M. Bettencourt, A particle-in-cell method for the simulation of plasmas based on an unconditionally stable field solver, Journal of Computational Physics, 326 (2016) 342-372.
- [11] B. Wang, et al., Modern gyrokinetic particle-in-cell simulation of fusion plasmas on top supercomputers, The International Journal of High Performance Computing Applications, 33 (2019) 168-188.
- [12] T. D. Arber, et al., Contemporary particle-in-cell approach to laser-plasma modelling, Plasma Physics and Controlled Fusion, 57 Article. 113001 (2015).
- [13] J. Chen and J Zhang, Impact of geometrical parameters on SGEMP responses in cylinder model, Nuclear Engineering and Technology, 54 (2022) 3415-3421.
- [14] H. Zhang, et al. Particle-in-cell simulations of low-pressure air plasma generated by pulsed x rays, Journal of Applied Physics, 130 Article. 173303 (2021).
- [15] Z. Xu, et al., A code verification for the cavity SGEMP simulation code LASER-SGEMP, IEEE Transactions on Nuclear Science, 68 (2021) 1251-1257.
- [16] Q. Lu, et al., Particle-in-cell simulations of whistler waves excited by an electron K distribution in space plasma, Journal of Geophysical Research Space Physics, 115 Article. A02213 (2010).
- [17] J. Chen, et al., 2D planar PIC simulation of space charge limited current with geometrical parameters, varying temporal-profile and initial velocities, IEEE ACCESS, 10 (2022) 28499-28508.
- [18] J. Wang, et al., A megawatt-level surface wave oscillator in Y-band with large oversized structure driven by annular relativistic electron beam, Scientific Reports, 8 Article. 6978

- (2018).
- [19] D. R. Welch, Fast hybrid particle-in-cell technique for pulsed-power accelerators, *Physical review accelerators and beams*, 23 Article. 110401 (2020).
 - [20] J. Derouillat, A. Beck, et al., Smilei : A collaborative, open-source, multi-purpose particle-in-cell code for plasma simulation, *Computer Physics Communications*, 222 (2018) 351-373.
 - [21] J.L Vay, A Almgren, J. Bell, et al., Warp-X: A new exascale computing platform for beam-plasma simulations. *Nuclear Instruments and Methods in Physics Research Section A: Accelerators, Spectrometers, Detectors and Associated Equipment*, 909 (2018) 476-479.
 - [22] H. Burau, R. Widera, et al., PIconGPU: A Fully Relativistic Particle-in-Cell Code for a GPU Cluster, *IEEE Transactions on Plasma Science*, 38 (2010) 2831 - 2839.
 - [23] J. Wang, et al., UNIPIC code for simulations of high power microwave devices, *Phys. Plasmas*, 16 Article. 033108 (2009).
 - [24] C. P. Ridgers, et al., Modelling gamma-ray photon emission and pair production in high-intensity laser-matter interactions, *Journal of Computational Physics*, 260 (2014) 273-285.
 - [25] K. Yee, Numerical solution of initial boundary value problems involving maxwell's equations in isotropic media, *IEEE Transactions on Antennas and Propagation*, 1 (1966) 302-307.
 - [26] D-Y. Na, Y. A. Omelchenko, H. Moon, B. V. Borges, F. L. Teixeira, Axisymmetric Charge-Conservative Electromagnetic Particle Simulation Algorithm on Unstructured Grids: Application to Microwave Vacuum Electronic Devices, *Journal of Computational Physics*, 346 (2017) pp. 295-317.
 - [27] D-Y. Na, H. Moon, Y. A. Omelchenko, and F. L. Teixeira, Relativistic extension of a charge-conservative finite element solver for time-dependent Maxwell-Vlasov equations, *Physics of Plasmas*, 25(1) Article. 013109 (2018).
 - [28] A. B. Langdon, On enforcing Gauss' law in electromagnetic particle-in-cell codes, *Computer Physics Communications* 70 (1992) 447-450.
 - [29] J. P. Verboncoeur, Symmetric Spline Weighting for Charge and Current Density in Particle Simulation, *Journal of Computational Physics*, 174 (2001) 421-427.
 - [30] T. Zh. Esirkepov, Exact charge conservation scheme for Particle-in-Cell simulation with an arbitrary form-factor, *Computer Physics Communications*, 135 (2001) 144-153.
 - [31] J. W. Eastwood, The virtual particle electromagnetic particle-mesh method, *Computer Physics Communications*, 64 (1991) 252-266.
 - [32] Y. Wang, J. Wang, Z. Chen, et al., Three-dimensional simple conformal symplectic particle-in-cell methods for simulations of high power microwave devices, *Computer Physics Communications*, 205 (2016) 1-12.
 - [33] O. D. Jefimenko, *Electricity and magnetism: an introduction to the theory of electric and magnetic fields*, Electret Scientific Co, Star City, W. Va, (1989).
 - [34] D. Griffiths, *Introduction to electrodynamics*, Prentice Hall, Upper Saddle River, N.J, (1999).
 - [35] J. Zhang, et al., JefiGPU: Jefimenko's equations on GPU, *Computer Physics Communications*, 276 Article. 108328 (2022).
 - [36] H. Wu, et al., ZMCintegral: A package for multi-dimensional Monte Carlo integration on multi-GPUs, *Computer Physics Communications*, 248 Article. 106962 (2020).
 - [37] R. Courant, K. Friedrichs and H. Lewy, On the partial difference equations of mathematical physics, *IBM Journal of Research and Development*, 11 (1967) 215-234.
 - [38] J. Berenger, A perfectly matched layer for the absorption of electromagnetic waves, *Journal of Computational Physics*, 114 (1994) 185-200.
 - [39] G. Mur, Absorbing boundary conditions for the finite-difference approximation of the time-domain electromagnetic-field equations, *IEEE Transactions on Electromagnetic Compatibility*, EMC-23(4) (1981) 377-382.

- [40] M. F Pasik, D. B Seidel, and R. W Lemke, A Modified Perfectly Matched Layer Implementation for Use in Electromagnetic PIC Codes, *Journal of Computational Physics*, 148 (1999) 125-132.
- [41] G. Jost, T.M. Tran, K. Appert, and S Wüthrich, Effect of electron-cyclotron instabilities on gyrotron beam quality, *Computer Physics Communications*, 100 (1997) 47-55.
- [42] J. Zhang, et al., Towards a full solution of the relativistic Boltzmann equation for quark-gluon matter on GPUs, *Physical Review D*, 102 Article. 074011 (2020).
- [43] Roden, J. A., and S. D. Gedney, Convolution PML (CPML): An efficient FDTD implementation of the CFS-PML for arbitrary media: *Microwave and Optical Technology Letters*, 27 (2000) 334-339.
- [44] J. Wang, Y. Wang, and D. Zhang, Truncation of open boundaries of cylindrical waveguides in 2.5-dimensional problems by using the convolutional perfectly matched layer, *IEEE Transactions on Plasma Science*, 34 (2006) 681-690.
- [45] J. Zhang, et al., Charge-dependent directed flows in heavy-ion collisions by Boltzmann-Maxwell equations, *Physical Review Research*, 4 (2022) Article. 033138.
- [46] O. Buneman and W. B. Pardo, *Relativistic Plasmas*, Benjamin, New York, (1968).
- [47] B. Goplin, et al., *Users Manual for MAGIC*, Mission Research Corporation Report No. MRC/WDC-R-068, Alexandria, VA, (1983).
- [48] G. G. Howes, Laboratory space physics: Investigating the physics of space plasmas in the laboratory, 25 Article. 055501 (2018).
- [49] G. Peng, et al., Two typical collective behaviors of the heavy ions expanding in cold plasma with ambient magnetic field, *Physics of Fluids*, 33 (2021) Article. 076602.
- [50] S. H. Brecht and D. J. Larson, The physics of ion decoupling in magnetized plasma expansions, *Journal of Geophysical Research: Space Physics*, 116 (2011) Article. A11310.
- [51] J. Chen, et al., Simulation of SGEMP using particle-in-cell method based on conformal technique, *IEEE Transactions on Nuclear Science*, 66 (2019) 820-826.
- [52] K.E. Lonngren, Expansion of an electron cloud, *Physical Letters A*, 59 (1976) 285-286.
- [53] P.J. Mardahl, J.P. Verboncoeur, Charge conservation in electromagnetic PIC codes; spectral comparison of Boris/DADI and Langdon-Marder methods, *Computer Physics Communications*, 106 (1997) 219-229.
- [54] Mohammad Ghorbanalilu, Elahe Abdollahzadeh and S.H. Rahbari, Particle-in-cell simulation of two stream instability in the non-extensive statistics, *Laser and Particle Beams*, 32 (2014) 399-407.
- [55] Hark Lee and Wei Cai, Ewald Summation for Coulomb Interactions in a Periodic Supercell, *Laser and Particle Beams*, 32 (2014) 399-407.